Euler–Euler simulations of condensing two-phase flows in mini-channel: Combination of a sub-grid approach and an interface capturing approach

Germain Davy, Etienne Reyssat, Stéphane Vincent, Stéphane Mimouni

Euler-Euler simulations of condensing two-phase flows in mini-channel: combination of a sub-grid approach and an interface capturing approach

G. Davy[a,b,c,*], Etienne Reyssat[c], Stéphane Vincent[b], Stéphane Mimouni[a]

[a] *R&D Division, Electricité de France (EDF), Chatou, France*
[b] *Laboratoire Modélisation et Simulation Multi-Echelle (MSME), CNRS, Université Paris-Est Créteil, Université Gustave Eiffel, Marne-la-Vallée, France*
[c] *Laboratoire Physique et Mécanique des Milieux Hétérogènes (PMMH), CNRS, ESPCI Paris, Université PSL, Sorbonne Université, Université Paris Diderot, Paris, France*

Abstract

A new model implemented in the neptune_cfd code is used to study steam condensation in the presence of air in a mini-channel of opening 100 µm. This model is the Full Generalized Large Interface Model. It combines a sub-grid approach and an interface capturing approach. The sub-grid approach is used to compute the small flow structures, which can be small bubbles or droplets, while the interface capturing approach is used to compute the large flow structures, which can be gas or liquid films, large bubbles or large drops. It is conceived to simulate a wide range of flow configurations, without the need for the grid cells to be smaller than the smallest flow structures. The results show that the model is able to reproduce all the flow patterns experimentally observed in mini-channels in the analysed range of control parameters. Both the pressure drop and the Nusselt number (dimensionless wall heat flux) are found to be in good agreement with experimental correlations from the literature.

Keywords: condensation, mini-channel, computational fluid dynamics, multi-regime, pressure drop, Nusselt number

1. Introduction

The understanding and modeling of two-phase flows in confined geometries like mini-channels and cracks is a major issue for many industries. Examples include the electronics, automotive, aeronautics and chemical industries (Chen et al., 2014; Da Riva et al., 2012; Ganapathy et al., 2013; Hu and Chao, 2007; Wu and Cheng, 2005; Yin et al., 2015; Zhang et al., 2016b; Zhao et al., 2015), with systems such as compact heat exchangers, micro-pumps and micro-reactors, but also the nuclear industry (Davy et al., 2020; Mimouni et al., 2019; Rastiello et al., 2015). Indeed, in a

*Corresponding author
Email address: germain.davy@univ-eiffel.fr (G. Davy)
URL: msme.u-pem.fr (G. Davy)

nuclear power plant, in the event of a loss-of-coolant accident, steam and fission products would be released in the containment building. In the case of a double wall concrete containment (no steel liner), the increase in pressure and temperature could lead to the opening of preexisting cracks and to the creation of new cracks (opening of the order of 100 µm) in the inner wall, through which gas and fission products could escape. Two phenomena could have an impact on the gas leakage rate. The first is steam condensation on the internal wall and inside the cracks, which could result in their clogging by drop, films and/or slugs. The second is concrete thermal deformation, which could result in variations in the crack opening.

The present work focuses on the first of the two phenomena described above, i.e., steam condensation in confined geometries. Recent numerical work on condensation in mini-channels is summarized in Table 1. Da Riva and Del Col (2011, 2012); Da Riva et al. (2012) carried out a series of studies on condensation of R134a (1,1,1,2-tetrafluoroethane) in a 1 mm diameter circular mini-channel. They found that, at high mass fluxes, the heat transfer coefficient (ratio of wall heat flux to difference in temperature between the solid surface and the surrounding fluid area) can only be predicted correctly if liquid turbulence is taken into account. Yin et al. (2015) studied condensation of water vapor in a 1 mm diameter circular mini-channel in the presence of a non-condensable gas (air, oxygen, helium or hydrogen). They found that the existence of a non-condensable gas led to a decrease in the interfacial mass transfer rate (mass exchanged at the gas-liquid interface per unit area and per unit time) and in the heat transfer coefficient. Zhang et al. (2016a,b, 2017) conducted a series of studies on condensation of R410A (mixture of difluoromethane and pentafluoroethane) in mini-channels of various shapes and sizes. They found that the heat transfer was stronger in flattened and helical microfin tubes than in smooth circular tubes. Based on the results obtained for smooth circular tubes, they proposed two new correlations, one for the frictional pressure drop and another for the heat transfer coefficient. Zhao et al. (2015) studied condensation of R22 (chlorodifluoromethane) in a 0.91 mm hydraulic diameter mini-channel. They developed a flow regime map and proposed new correlations for the frictional pressure drop and the heat transfer coefficient. In all these studies, the flow regime is annular. The volume-of-fluid (VOF) method is used under steady-state assumption. The mass and energy transfer terms, computed using the model of Lee (1980), are based on a constant that is problem-dependent.

Two other studies worth mentioning are those of Chen et al. (2014) and Ganapathy et al. (2013). Chen et al. (2014) studied condensation of FC-72 (perfluorohexane) in a 1 mm hydraulic diameter mini-channel. They were able to observe various flow regimes, including smooth annular, wavy annular, slug and bubbly flow. They found these flow patterns to be consistent with the experimental data of Kim et al. (2012) and Wang et al. (2002). Ganapathy et al. (2013) investigated condensation of R134a (1,1,1,2-tetrafluoroethane) in a 0.1 mm hydraulic diameter mini-channel. They observed flow patterns similar to those mentioned previously (with, in addition, droplet flow). They found

the frictional pressure drop and the Nusselt number (dimensionless heat transfer coefficient) to be in good agreement with a number of correlations from the literature. In these two studies, the VOF method is also used. Unlike previously, no steady-state assumption is made. Concerning phase change, the model used by Chen et al. (2014) is similar to that of Lee (1980). The model used by Ganapathy et al. (2013) is close to that presented in Section 2.4.2.

It is important to note that, in the studies mentioned previously, all the gas-liquid interfaces are supposed to be fully resolved, even the smallest ones. The main drawback of this kind of approach is its computational cost, since it requires the use of very fine meshes and thus very small time steps.

Table 1: Computational condensation studies found in the literature. 2D stands for "two dimensions", 3D for "three dimensions", A for "annular flow", B for "bubbly flow", C for "circular cross-section", CF for "circular flattened cross-section", D for "droplet flow", H for "horizontal", I for "infinite cross-section", M for "microfin tube", NCG for "non-condensable gases", R for "rectangular cross-section", S for "slug flow", SC for "semi-circular cross-section", V for "vertical" and VOF for "volume-of-fluid method".

Authors	Orientation, geometry, diameter, fluid	Regime(s)	Approach
Chen et al. (2014)	H, R, 1 mm, FC-72	D, A, S, B	3D, VOF
Da Riva and Del Col (2011)	H and V, C, 1 mm, R134a	A	3D, VOF, steady
Da Riva and Del Col (2012)	H, C, 1 mm, R134a	A	3D, VOF, steady
Da Riva et al. (2012)	H, C, 1 mm, R134a	A	3D, VOF, steady
Ganapathy et al. (2013)	H, I, 0.1 mm, R134a	A, S, B	2D, VOF
Yin et al. (2015)	H, C, 1 mm, water and NCG	A	3D, VOF, steady
Zhang et al. (2016a)	H, C, 0.25-4 mm, R410A	A	3D, VOF, steady
Zhang et al. (2016b)	H, CF, 3.78 mm, R410A or R134a	A	3D, VOF, steady
Zhang et al. (2017)	H, C and M, 4.54 mm, R410A	A	3D, VOF, steady
Zhao et al. (2015)	n/a, SC, 0.91 mm, R22	A	3D, VOF, steady

The present work aims to assess the ability of a new model implemented in the neptune_cfd code[1] to correctly predict steam condensation and resulting flow patterns in mini-channels. This model is the Full Generalized Large Interface Model (Davy et al., 2020). It combines a sub-grid approach and an interface capturing approach. The sub-grid approach is used to compute the small flow structures, which can be small bubbles or droplets, while the interface capturing approach is used to compute the large flow structures, which can be gas or liquid films, large bubbles or large drops. It is conceived to simulate a wide range of flow configurations, without the need for the grid cells to be smaller than the smallest flow structures. It also has the advantage that no empirical constant is used for phase change.

[1]The neptune_cfd code is jointly developed by EDF, CEA, Framatome and IRSN

The document is organized as follows. The balance equations solved by the code are given in Section 2.1. The model employed is presented in Sections 2.2 to 2.4. The numerical setup and the assumptions done are detailed in Section 3. In Section 4, the flow patterns obtained by simulation are qualitatively compared with experimental views from the literature. In addition, the pressure drop and the Nusselt number are quantitatively compared with experimental correlations. Conclusions are drawn in Section 5.

2. Modeling strategy

2.1. Governing equations

Two computational fields are used: a gas field (g) and a liquid field (l). The following mass, momentum and energy balance equations are considered for $k = g$ and $k = l$:

$$\frac{\partial}{\partial t}\left(\alpha_k \rho_k\right) + \underline{\nabla} \cdot \left(\alpha_k \rho_k \underline{U}_k\right) = \Gamma_{p\to k} + \Gamma_{w\to k}\,, \tag{1}$$

$$\frac{\partial}{\partial t}\left(\alpha_k \rho_k \underline{U}_k\right) + \underline{\nabla} \cdot \left(\alpha_k \rho_k \underline{U}_k \otimes \underline{U}_k\right) = -\alpha_k \underline{\nabla} P + \underline{\nabla} \cdot \left[\alpha_k \left(\underline{\underline{\Sigma}}_k + \underline{\underline{\Sigma}}_k^{Re}\right)\right] + \alpha_k \rho_k \underline{g} + \underline{I}_{p\to k}\,, \tag{2}$$

$$\frac{\partial}{\partial t}\left(\alpha_k \rho_k H_k\right) + \underline{\nabla} \cdot \left(\alpha_k \rho_k H_k \underline{U}_k\right) = \alpha_k \frac{\partial P}{\partial t} - \underline{\nabla} \cdot \left(\alpha_k \underline{Q}_k + \underline{Q}_k^{Re}\right) + \Gamma_{p\to k} H_k + \Pi_{p\to k} + \varphi_{w\to k}\,. \tag{3}$$

H_k, $\underline{Q}_k$, $\underline{Q}_k^{Re}$, $\underline{U}_k$, α_k, ρ_k, $\underline{\underline{\Sigma}}_k$ and $\underline{\underline{\Sigma}}_k^{Re}$ are, respectively, the average total enthalpy, heat flux density, turbulent heat flux density, average velocity, volume fraction, density, viscous stress tensor and Reynolds stress tensor of phase k. $\underline{g}$ is the gravity. P is the pressure (assumed to be the same for both fields). $\underline{I}_{p\to k}$, $\Gamma_{p\to k}$, and $\Pi_{p\to k}$ denote, respectively, the momentum, mass and energy transfers from phase p to phase k. $\Gamma_{w\to k}$ denotes the mass contribution to phase k induced by wall condensation and $\varphi_{w\to k}$ denotes the energy contribution to phase k induced by wall condensation and/or wall sensible heat transfer. These equations are solved with the neptune_cfd code. This code is based on the finite volume discretization method and uses a SIMPLE (Semi-Implicit Method for Pressure Linked Equations) algorithm as solution procedure.

2.2. The Full Generalized Large Interface Model

The models available in the code are listed in Table 2. The model used in the present work is the newly developed Full Generalized Large Interface Model (FGLIM). This model uses both a sub-grid approach, like in the Standard Dispersed Model, and an interface capturing approach, like in the Large Interface Model, and switches between the two according to the composition of the considered cell. Closures for sub-grid droplets, corresponding to Case 1 in Fig. 1, are applied in the cells with a liquid volume fraction lower than α_l^{lim}, and closures for sub-grid bubbles, corresponding to Case 3 in Fig. 1, are applied in the cells with a liquid volume fraction greater than α_l^{lim}. In both cases, the interface is not explicitly modeled. In a cell, all the droplets/bubbles have the

same diameter, velocity and temperature. The diameter is obtained by solving a transport equation on the interfacial area. Closures for large interfaces (i.e., interfaces “captured" by several cells), corresponding to Case 2 in Fig. 1, are applied in the cells with a liquid volume fraction between α_l^{inf} and α_l^{sup}. An additional equation, called interface sharpening equation, is solved to maintain constant the large interface thickness. However, unlike in codes based on the one-fluid formalism, no additional equation is required for large interface advection, since a mass balance is solved for each phase (see Section 2.1). To avoid superimposing closures corresponding to the sub-grid approach and to the interface capturing approach, a weighting is done between the closures for the sub-grid droplets (respectively, sub-grid bubbles) and the closures for the large interfaces in the cells with a liquid volume fraction between α_l^{inf} and α_l^{lim} (respectively, between α_l^{lim} and α_l^{sup}).

The FGLIM can be seen as an extension of the Generalized Large Interface Model, the latter including Cases 2 and 3 but not Case 1 and using different closures laws for mass, momentum and energy. It worth noting that the two models completely rely on the volume fraction. Cells with $\alpha_l > \alpha_l^{lim}$ cannot be treated as droplets, cells with $\alpha_l < \alpha_l^{lim}$ cannot be treated as bubbles and cells with $\alpha_l < \alpha_l^{inf}$ or $\alpha_l > \alpha_l^{sup}$ cannot be treated as large interfaces. It is also worth noting that the FGLIM has already been validated on several test cases, involving droplets, bubbles and/or large interfaces (not provided here for consistency, since they do not involve mini-channels). Different combinations for α_l^{inf}, α_l^{lim} and α_l^{sup} were tested and the best results were obtained for $\alpha_l^{inf} = 0.4$, $\alpha_l^{lim} = 0.5$ and $\alpha_l^{sup} = 0.6$. Therefore, these values are kept for use in the present work.

Table 2: Models for gas-liquid flows available in the neptune_cfd code. FGLIM stands for “Full Generalized Large Interface Model”, GLIM for “Generalized Large Interface Model”, LBM for “Large Bubble Model”, LI for “large interface”, LIM for “Large Interface Model” and SDM for “Standard Dispersed Model”.

Model	Reference(s)	Bubbles	Droplets	LI
SDM (bubbles)	Mimouni et al. (2010, 2011)	Yes	No	No
SDM (droplets)	Mimouni et al. (2010, 2011)	No	Yes	No
LIM	Coste and Lavieville (2008, 2009); Coste (2013)	No	No	Yes
LBM	Denèfle et al. (2015); Fleau et al. (2015)	Yes	No	Yes
GLIM	Mérigoux et al. (2016); Mer et al. (2018)	Yes	No	Yes
FGLIM	Davy et al. (2020)	Yes	Yes	Yes

2.3. Closure laws for bubbles and droplets

2.3.1. Interfacial momentum transfers for bubbles and droplets

As in the Standard Dispersed Model, for bubbles and droplets, the momentum transfers read as the sum of a drag force $\underline{F}^D$, an added mass force $\underline{F}^{AM}$, a lift force $\underline{F}^L$, a wall force $\underline{F}^W$ and a

turbulent dispersion force $\underline{F}^{TD}$:

$$\underline{I}_{c\to d} = -\underline{I}_{d\to c} = \underline{F}^{D}_{c\to d} + \underline{F}^{AM}_{c\to d} + \underline{F}^{L}_{c\to d} + \underline{F}^{W}_{c\to d} + \underline{F}^{TD}_{c\to d}\,, \tag{4}$$

where the subscript c stands for “continuous" and the subscript d for “dispersed". In the following, for droplets ($c = g$ and $d = l$), only the drag force is taken into account. The drag coefficient is obtained from the correlation of Gobin et al. (2003). For bubbles ($c = l$ and $d = g$), only the drag, added mass and lift forces are taken into account. The drag, added mass and lift coefficients are obtained from the correlations of Ishii and Zuber (1979), Zuber (1964) and Tomiyama et al. (2002), respectively. Expressions of these forces are given in Table 3, in which d_d refers to the droplet/bubble diameter. It is given by: $d_d = \frac{6\alpha_d}{a_d^{int}}$, with a_d^{int} the interfacial area concentration. The latter is obtained by solving an additional transport equation, which takes into account size variation due to phase change for droplets (Mimouni et al., 2010, 2011) and due to phase change, coalescence and break-up for bubbles (Guelfi et al., 2007). The model of Ruyer et al. (2007) is used for bubble coalescence and break-up.

Table 3: Expressions used for the drag, added mass and lift forces. $C_X = \{C_D, C_{AM}, C_L\}$.

Force	Expression	C_X for droplets	C_X for bubbles
$\underline{F}^{D}_{c\to d}$	$-\frac{6}{8}\frac{\alpha_d}{d_d}C_D\rho_c\left\|\underline{U}_d - \underline{U}_c\right\|(\underline{U}_d - \underline{U}_c)$	Gobin et al. (2003)	Ishii and Zuber (1979)
$\underline{F}^{AM}_{c\to d}$	$-\alpha_d C_{AM}\rho_c\left(\frac{D\underline{U}_d}{Dt} - \frac{D\underline{U}_c}{Dt}\right)$	–	Zuber (1964)
$\underline{F}^{L}_{c\to d}$	$-\alpha_d C_L\rho_c(\underline{U}_d - \underline{U}_c)\wedge(\underline{\nabla}\wedge\underline{U}_c)$	–	Tomiyama et al. (2002)

2.3.2. Interfacial energy and mass transfers for droplets

For droplets, the energy and mass transfers from the liquid to the gas are computed using the expressions proposed by Mimouni et al. (2010, 2011):

$$\Pi_{l\to g} = \frac{6\alpha_l}{d_l^2}\cdot Nu_g\cdot\lambda_g\cdot(T_l - T_g)\,, \tag{5}$$

$$\Gamma_{l\to g} = \frac{6\alpha_l}{d_l^2}\cdot Sh_g\cdot D\cdot(\rho_{s,sat}(T_l) - Y_s\rho_g)\,. \tag{6}$$

D is the diffusion coefficient of steam in air. It is obtained from the correlation of Oran and Boris (1981): $D = 4.88\times10^{-4}\frac{T^{\frac{3}{2}}}{P}$, with T computed as an average between the gas temperature T_g and the liquid temperature T_l. Nu_g and Sh_g are the gas Nusselt and Sherwood numbers. They are obtained from the correlations of Ranz and Marshall (1952): $Nu_g = 2 + 0.56Re_{pl}^{\frac{1}{2}}Pr_g^{\frac{1}{3}}$ and $Sh_g = 2 + 0.56Re_{pl}^{\frac{1}{2}}Sc_g^{\frac{1}{3}}$, with $Re_{pl} = \frac{\rho_g\left\|\underline{U}_g - \underline{U}_l\right\|d_l}{\mu_g}$ the liquid particle Reynolds number, $Pr_g = \frac{\mu_g Cp_g}{\lambda_g}$ the gas Prandtl number and $Sc_g = \frac{\mu_g}{\rho_g D}$ the gas Schmidt number. Cp_g, λ_g and μ_g are the gas heat capacity, thermal conductivity and molecular viscosity. Y_s and $\rho_{s,sat} = \rho_s(P_{sat}, T)$ are the steam mass fraction and saturation density. The steam mass fraction is given by: $Y_s = 1 - Y_a$, with Y_a

the air mass fraction, obtained by solving an additional transport equation (Mimouni et al., 2010, 2011).

The energy and mass transfers from the gas to the liquid are deduced from:

$$\Pi_{g\to l} = -\Pi_{l\to g} - \Gamma_{l\to g} H_{lat}\,, \tag{7}$$

$$\Gamma_{g\to l} = -\Gamma_{l\to g}\,. \tag{8}$$

H_{lat} is the latent heat. It is given by: $H_{lat} = H_g - H_l$.

2.3.3. Interfacial energy and mass transfers for bubbles

For bubbles, the energy transfer from the gas to the liquid is computed using the expression proposed by Manon (2000):

$$\Pi_{g\to l} = \frac{6\alpha_g}{d_g^2} \cdot Nu_l \cdot \lambda_l \cdot (T_{sat} - T_l)\,. \tag{9}$$

Like the gas Nusselt number, the liquid Nusselt number Nu_l is obtained from the correlation of Ranz and Marshall (1952): $Nu_l = 2 + 0.56 Re_{pg}^{\frac{1}{2}} Pr_l^{\frac{1}{3}}$, with $Re_{pg} = \frac{\rho_l \left\| \underline{U}_g - \underline{U}_l \right\| d_g}{\mu_l}$ the gas particle Reynolds number and $Pr_l = \frac{\mu_l Cp_l}{\lambda_l}$ the liquid Prandtl number. Cp_l, λ_l and μ_l are the liquid heat capacity, thermal conductivity and molecular viscosity. T_{sat} is the saturation temperature.

The energy transfer from the liquid to the gas is computed as:

$$\Pi_{l\to g} = \alpha_g \alpha_l \frac{\rho_g Cp_g}{\tau} \left(T_{sat} - T_g\right)\,. \tag{10}$$

In fact, this term is a penalty term, whose purpose is that the gas temperature remains close to the saturation temperature. Therefore, the characteristic time τ has no physical meaning. It is chosen equal to the time step, so that $T_g \approx T_{sat}$ is met at each iteration in cells with bubbles.

The mass transfers are deduced from:

$$\Gamma_{g\to l} = -\Gamma_{l\to g} = \frac{\Pi_{g\to l} + \Pi_{l\to g}}{H_{lat}}\,. \tag{11}$$

2.3.4. Wall energy and mass transfers for droplets

At the wall, the mass transfers are computed using the expression proposed by Mimouni et al. (2010, 2011):

$$\Gamma_{w\to g} = -\Gamma_{w\to l} = \frac{S}{V} \cdot n_{site} \cdot \pi \cdot Sh_g \cdot D \cdot \frac{d_l}{2} \cdot \left(\rho_{s,sat}\left(T_w\right) - Y_s \rho_g\right)\,. \tag{12}$$

n_{site} is the number of droplets formed at nucleation sites per unit area. It is given by: $n_{site} = \frac{4A_l}{\pi d_l^2}$, with A_l the fraction of area affected by the liquid. S/V is the ratio of the surface of the boundary face to the volume of the boundary cell. T_w is the wall temperature.

The energy transfers are computed as:

$$\varphi_{w\to g} = \varphi_{cond} + \varphi_{sp,g}\,, \tag{13}$$

$$\varphi_{w\to l} = \varphi_{sp,l}\,. \tag{14}$$

φ_{cond} is the condensation flux. It is deduced from: $\varphi_{cond} = \Gamma_{w\to g} H_{lat}$. $\varphi_{sp,g}$ and $\varphi_{sp,l}$ are the single-phase gas and liquid heat fluxes. They are obtained from: $\varphi_{sp,g} = (1 - A_l)\, h_{loc,g}\,(T_w - T_g)$ and $\varphi_{sp,l} = A_l h_{loc,l}\,(T_w - T_l)$, with $h_{loc,g}$ and $h_{loc,l}$ the gas and liquid local heat transfer coefficients. These coefficients are given by: $h_{loc,k} = \frac{\lambda_k}{\Delta} \cdot c_k$, with Δ the distance from the wall to the center of the boundary cell and c_k a dimensionless rescaling factor equal to unity in the laminar flow regime and provided by an analytical wall function in the turbulent flow regime.

2.4. Closure laws for large interfaces

2.4.1. Interfacial momentum transfers

For large interfaces, the momentum transfers read as the sum of a generalized drag force $\underline{F}^D$, which allows to couple the gas and liquid velocities, and a surface tension force $\underline{F}^{ST}$:

$$\underline{I}_{l\to g} = -\underline{I}_{g\to l} + \underline{F}^{ST}_{tot} = \underline{F}^{D}_{l\to g} + \underline{F}^{ST}_{g}\,. \tag{15}$$

$\underline{F}^D$ is computed using a combination of the expression proposed by Coste (2013) in the framework of the Large Interface Model and the expression proposed by Mimouni et al. (2017) in the framework of the Large Bubble Model:

$$\underline{F}^{D}_{l\to g} = \alpha_g \alpha_l \left(f^\theta_l + \theta\left(f^\theta_g - f^\theta_l\right)\right)\left(\underline{U}_l - \underline{U}_g\right)\,. \tag{16}$$

f^θ_l, f^θ_g and θ are given by: $f^\theta_l = 18\frac{\mu_g}{d_l^2}\left(1 + 0.15 Re_{pl}\right)$, $f^\theta_g = 18\frac{\mu_l}{d_g^2}\left(1 + 0.15 Re_{pg}\right)$ and $\theta = \frac{1}{2}\left(1 - \cos\left(\pi\alpha_l\right)\right)$, with Re_{pl} and Re_{pg} defined in Section 2.3.2 and Section 2.3.3, respectively. Originally introduced in the Large Bubble Model, $\underline{F}^{ST}$ is computed the same way as in this model, i.e, using the Continuum Surface Force approach of Brackbill et al. (1992):

$$\underline{F}^{ST}_{tot} = -\sigma \underline{\nabla} \cdot \left(\underline{n}_l\right) \underline{\nabla}\,\alpha_l\,. \tag{17}$$

$\underline{n}_l$ is the interface normal pointing towards g. It is given by: $\underline{n}_l = \frac{\underline{\nabla}\,\alpha_l}{\|\underline{\nabla}\,\alpha_l\|}$. σ is the surface tension. $\underline{F}^{ST}_{tot}$ is split between the gas and the liquid by weighting by the volume fraction:

$$\underline{F}^{ST}_{k} = \alpha_k \underline{F}^{ST}_{tot}\,. \tag{18}$$

In order to maintain constant interface thickness, which is required to accurately compute the interface normal, an additional equation, called interface-sharpening equation, is solved for each field k in the cells assumed to contain a portion of large interface:

$$\frac{\partial \alpha_k}{\partial \tau} + \underline{\nabla} \cdot \left(\alpha_k\left(1 - \alpha_k\right)\underline{n}_k\right) = \varepsilon \underline{\nabla}^2\,\alpha_k\,, \tag{19}$$

with $\Delta\tau = \frac{\Delta x}{32}$ and $\varepsilon = \frac{\Delta x}{2}$, corresponding to a thickness of 5 cells of size Δx.

2.4.2. Interfacial energy and mass transfers

For large interfaces, the energy transfers are computed using the expressions proposed by Fleau (2017) in the framework of the Large Bubble Model:

$$\Pi_{l\to g} = \alpha_g \alpha_l \lambda_g \underline{\nabla} T_g \cdot \underline{\nabla} \alpha_g \,, \tag{20}$$

$$\Pi_{g\to l} = \alpha_g \alpha_l \lambda_l \underline{\nabla} T_l \cdot \underline{\nabla} \alpha_l \,. \tag{21}$$

In the neptune_cfd code, the gradients are computed using a five-cell stencil. Fleau (2017) showed that this could be a problem for temperature. Indeed, for a given interface cell, the stencil used to compute, e.g., the liquid temperature gradient could include cells with only gas, in which the liquid temperature does not make sense. As an alternative, the author proposed the following modified expression, based on the fact that condensing steam or evaporating liquid must be at saturation temperature: $\underline{\nabla} T_k = (T_{sat} - T_k)\left(\frac{\underline{e}_x}{\Delta x} + \frac{\underline{e}_y}{\Delta y} + \frac{\underline{e}_z}{\Delta z}\right)$.

In the present work, since air is present, Eqs. (20) and (21) are weighted by Y_s. The resulting expressions are successfully validated by comparison with analytical data in a 1D phase change case based on the Stefan problem. However, for the sake of brevity, the results are not provided.

The mass transfers are deduced from the same equation as Eq. (11).

3. Problem setup

3.1. Computational domain and boundary conditions

An air-steam mixture is injected into the two-dimensional mini-channel of opening $d = 100\,\mu\text{m}$ and length $l = 3\,\text{cm}$ presented in Fig. 2. Flow rate, temperature and composition boundary conditions are imposed at the inlet, a pressure boundary condition is imposed at the outlet and a temperature boundary condition is imposed at the walls. Values used for these boundary conditions are given in Table 4. The outlet pressure P^{out} is set to 140 bar. Indeed, the final purpose is to assess the performance of the FGLIM at both low and high pressures, but the present work is restricted to high pressures. The air inlet mass fraction Y_a^{in} is set to 1 %. This low value aims to prove the ability of the FGLIM to take into account non-condensable gases while ensuring an important level of condensation. The gas inlet temperature T_g^{in} is set to $T_{sat} + 12\,\text{K}$ and the wall temperature T_w to either $T_{sat} - 15\,\text{K}$ or $T_{sat} - 25\,\text{K}$ (an exception is made for Calculation 0, which will be used for a single-phase flow verification; in this calculation, to avoid the formation of liquid, both T_g^{in} and T_w are set above T_{sat}). The gas inlet mass flow rate per unit area G is varied between 20 and $50\,\text{kg}\,\text{m}^{-2}\,\text{s}^{-1}$, to be able to observe a wide range of flow regimes. The physical properties are automatically computed using the CATHARE tables (Emonot et al., 2011). For the sake of information, the values at saturation are provided in Table 5. An adaptive time-stepping strategy is adopted. The maximum Courant and Fourier numbers, defined as $\|\underline{U}_k\|\frac{\Delta t}{\Delta x}$ and $\frac{\lambda_k}{\rho_k C p_k}\frac{\Delta t}{\Delta x}$, with Δt the time step and Δx the grid spacing, are set to 1 and 10 for both the gas and the liquid.

Table 4: Boundary conditions values for the various calculations performed in the present work. G the (gas inlet) mass flow rate per unit area, T_g^{in} the gas inlet temperature, P^{out} the outlet pressure and T_w the wall temperature.

Calculation number	Inlet		Walls
	G [kg m^{-2} s^{-1}]	T_g^{in} [K]	T_w [K]
0	20	650	620
1	20	622	595
2	30	622	595
3	40	622	595
4	50	622	595
5	20	622	585
6	30	622	585
7	40	622	585
8	50	622	585

Table 5: Physical properties at saturation. During the computation, the physical properties are automatically computed using the CATHARE tables (Emonot et al., 2011).

Property	$k = g$	$k = l$	Two phases
σ [N m^{-1}]	–	–	7.2×10^{-3}
λ_k [W m^{-1} K]	0.0707	0.472	–
μ_k [Pa s]	2.29×10^{-5}	8.14×10^{-5}	–
ρ_k [kg m^{-3}]	86.8	624	–
Cp_k [J kg^{-1} K^{-1}]	11 424	7752.6	–

3.2. Turbulence

In the present work, the gas and liquid Reynolds numbers are defined as:

$$Re_g = \frac{G x_g D_h}{\mu_g}, \tag{22}$$

$$Re_l = \frac{G\,(1 - x_g)\,D_h}{\mu_l}, \tag{23}$$

with $D_h = 2d$ the hydraulic diameter and x_g the flow quality, i.e., the ratio of vapor mass flow rate to total mass flow rate (see Section 3.6 in the following). An estimation of the gas Reynolds number at the inlet (where $x_g = 1$) Re_g^{in} is given in Table 6. For all the calculations, Re_g^{in} is far below the critical value of about 2000 for smooth circular pipes, above which the flow is considered to be turbulent. Therefore, no turbulence model is used for the gas field. No turbulence model is used for the liquid field either, since Re_l is expected to be lower than Re_g.

Table 6: Estimation of the gas Reynolds number (Eq. (22)) at the inlet.

Calculation number	0	1	2	3	4	5	6	7	8
Re_g^{in}	174	174	261	348	435	174	261	348	435

3.3. Gravity, roughness and wettability

Gravity is neglected. Indeed, the Eötvos number, defined as the ratio of gravitational to surface tension forces, is below the critical value of 0.88 proposed by Suo and Griffith (1964). Other criteria can be found in the literature (Brauner and Moalem-Maron, 1992; Cornwell and Kew, 1993), but this one is the most restrictive.

In the following, the results are compared with experimental correlations. Most of the experiments have used slightly rough and slightly hydrophilic surfaces. In the present work, for the sake of simplicity, roughness is neglected. Concerning wettability, for the large interfaces, a neutral contact angle of 90° is used. The advantage is that no contact angle model is required, the value of 90° being enforced via the null flux condition applied by the code to the volume fraction at the wall.

3.4. Mesh

A mesh convergence study is performed. Four Cartesian meshes are considered. To maintain a constant interface resolution, cubic cells are used. The number of cells in the x-direction N_x is varied between 10 and 30. Calculation 4 is used for comparison between the various meshes. The quantities of interest are the gas and liquid volume fractions, velocities and temperatures. These are averaged over time according to the following formulas: $\alpha_k = \langle \alpha_k \rangle$, $U_k = {}^{\langle \alpha_k \rho_k U_k \rangle}/_{\langle \alpha_k \rho_k \rangle}$ and $T_k = {}^{\langle \alpha_k \rho_k C p_k T_k \rangle}/_{\langle \alpha_k \rho_k C p_k \rangle}$, where $\langle \cdot \rangle$ denotes the time average. The results are shown in Fig. 3 for the gas phase. Convergence is reached for $N_x = 25$. Indeed, the profiles obtained with $N_x = 30$ are almost the same. Therefore, the mesh corresponding to $N_x = 25$ is kept for use in subsequent calculations. It ensures that the hydrodynamic and thermal boundary layers are properly solved. It is worth noting that, with this mesh, the time steps used by the code, resulting from the conditions on the Courant and Fourier numbers set in Section 3.1, are of the order of 10^{-6} s, which is very small. It is also worth noting that the models used for dynamics and phase change (presented in Sections 2.3 and 2.4) act differently according to the mesh resolution. However, the present results show that, once convergence is reached, similar levels of volume fraction, velocity and temperature are obtained.

3.5. Averaging procedure

In the following, the correlations to which are compared the results are one-dimensional correlations. Therefore, the problem variables are averaged over the cross-section. The expressions used

are given in Table 7. An area-weighted average is performed for volume fraction, surface tension and pressure. A volume-fraction-weighted average is performed for thermal conductivity, viscosity, density and specific heat capacity, to take into account only the regions where phase k is present. A volume-fraction- and density-weighted average is performed for velocity, since the conserved quantity is $\alpha_k \rho_k U_k$. A volume-fraction-, density- and heat-capacity-weighted average is performed for temperature, since the conserved quantity is $\alpha_k \rho_k H_k = \alpha_k \rho_k C p_k T_k$.

Table 7: One-dimensional quantities used in the following.

ϕ_k	Cross-sectional averaged ϕ_k
α_k, σ, P	$\frac{1}{d}\int_x \phi_k \mathrm{d}x$
λ_k, μ_k, ρ_k, Cp_k	$\frac{\int_x \alpha_k \phi_k \mathrm{d}x}{\int_x \alpha_k \mathrm{d}x}$
$U_{k,y}$	$\frac{\int_x \alpha_k \rho_k \phi_k \mathrm{d}x}{\int_x \alpha_k \rho_k \mathrm{d}x}$
T_k	$\frac{\int_x \alpha_k \rho_k C p_k \phi_k \mathrm{d}x}{\int_x \alpha_k \rho_k C p_k \mathrm{d}x}$

3.6. Flow quality

Another quantity used in the following is the flow quality, defined as the ratio of vapor mass flow rate to total mass flow rate:

$$x_g = \frac{\int_x \alpha_g \rho_g U_{g,y} \mathrm{d}x}{\int_x \left(\alpha_g \rho_g U_{g,y} + \alpha_l \rho_l U_{l,y}\right) \mathrm{d}x} \,. \tag{24}$$

Using the cross-sectional averaged quantities in Table 7, Eq. (24) can be rewritten as:

$$x_g = \left(1 + \frac{U_{l,y}}{U_{g,y}} \frac{\alpha_l}{\alpha_g} \frac{\rho_l}{\rho_g}\right)^{-1} \,. \tag{25}$$

A usual assumption is that the ratio of gas to liquid velocity, called slip ratio, is unity. The flow quality then simply corresponds to the static vapor quality (vapor mass fraction). This assumption is valid for flow regimes like droplet flow and bubbly flow, but is not valid for flow regimes like slug/plug flow, where there is a liquid film surrounding the vapor slugs. In the present work, as the latter flow regime is expected to occur, no assumption is made on the slip ratio.

3.7. Single-phase flow verification

Before detailing the results for two-phase flow, a verification is first performed for single-phase flow. The purpose is to ensure that single-phase heat transfer is correctly computed and to help understanding the results provided in the following. Calculation 0, in which no liquid is formed, is used. The quantity considered is the Nusselt number, which, in the present section, is computed as:

$$Nu_{sp,g} = \frac{h_{sp} D_h}{\lambda_g} \,, \tag{26}$$

with $h_{sp,g}$ the single-phase gas heat transfer coefficient, obtained from:

$$h_{sp,g} = \frac{\varphi_{sp,g}}{T_w - T_g} \,. \tag{27}$$

$\varphi_{sp,g}$, T_w and T_g are given, respectively, in Section 2.3.4, Table 4 and Table 7. Fig. 4 shows $Nu_{sp,g}$ as a function of ${}^{4y}/_{Re_g Pr_g D_h}$. Two regions can be distinguished: a region in which $Nu_{sp,g}$ decreases, corresponding to the development of the hydrodynamic and thermal boundary layers and referred to as hydrodynamic and thermal developing region, and a region in which $Nu_{sp,g}$ is constant, referred to as fully developed region. A good agreement is obtained with the analytical solution of Kays and Crawford (1993):

$$Nu_{sp,g} = 7.54 \,, \tag{28}$$

which is valid only in the fully developed region. Fig. 5 shows ${}^{1}/_{y} \int_0^y Nu_{sp,g} \mathrm{d}y'$ as a function of ${}^{4y}/_{Re_g Pr_g D_h}$. A good agreement is obtained with the analytical solution of Mercer et al. (1967):

$$\frac{1}{2y} \int_0^y Nu_{sp,g} \mathrm{d}y' = 3.77 + \frac{0.066 \left(\frac{Re_g Pr_g D_h}{4y} \right)^{1.2}}{1 + 0.1 Pr_g^{0.87} \left(\frac{Re_g Pr_g D_h}{4y} \right)^{0.7}} \,, \tag{29}$$

which is valid in both the hydrodynamic and thermal developing region and the fully develop region. Note that it is consistent with Eq. (28) ($2 \times 3.77 = 7.54$). These results indicate that single-phase heat transfer is correctly computed. Two-phase heat transfer is investigated in the following.

4. Results

4.1. Flow patterns

4.1.1. Droplet flow regime

The droplet flow regime is observed in all the calculations performed. It is shown in Fig. 6a. It is characterized by the nucleation of small droplets on the walls. Once formed, these droplets are entrained by the gas and slide along the walls. They are sub-grid droplets, which means that, at this location, the model uses the closures in Sections 2.3.1, 2.3.2 and 2.3.4.

4.1.2. Smooth and wavy annular flow regimes

The smooth and wavy annular flow regimes are also observed in all the calculations performed. As shown in Figs. 6b and 6c, the liquid flows on the walls as a film while the gas flows in the center. The two regimes can be distinguished by the shape of the interfaces, flat in one case and wavy in the other. Waves might result from a Kelvin-Helmholtz instability (Carey, 1992). Unlike in the droplet flow regime, the interfaces can be distinguished. Therefore, at this location, the model uses the closures in Section 2.4.

4.1.3. Slug flow regime

The length of the zone in which the previous flow regimes occur increases with flow rate. As a consequence, the slug flow regime is only observed in Calculations 1, 2, 5 and 6. It is shown in Fig. 6d. It is characterized by an alternation between large bubbles and liquid slugs, the liquid slugs resulting from the merging of two high-amplitude waves (see Fig. 7). Like in the smooth and wavy annular flow regimes, the interfaces can be distinguished, which means that, at this location, the model uses the closures in Section 2.4.

4.1.4. Comparison with experimental flow patterns

A qualitative comparison is made with the experiments of Hu and Chao (2007) and Wu and Cheng (2005). The channel geometry used in these experiments is close to that of the present work (hydraulic diameter between 73 and 237 µm and length of 2.8 cm for Hu and Chao (2007); hydraulic diameter of 82.8 µm and length of 3 cm for Wu and Cheng (2005)). The working fluid is the same. However, the operating conditions are different. Flow regimes similar as those mentioned previously are observed, which indicates that the model is able to capture all the flow regimes that would occur in a real system.

4.2. Frictional pressure drop

4.2.1. Computation and correlations used for comparison

The frictional pressure drop is quantified using the model of Lockhart and Martinelli (1947), in which:

$$\phi_l^2 = \frac{\left(\frac{dP}{dy}\right)_f}{\left(\frac{dP}{dy}\right)_{f,l}}, \tag{30}$$

$$\phi_g^2 = \frac{\left(\frac{dP}{dy}\right)_f}{\left(\frac{dP}{dy}\right)_{f,g}}, \tag{31}$$

$$X = \sqrt{\frac{\phi_g^2}{\phi_l^2}}. \tag{32}$$

ϕ_l^2 and ϕ_g^2 are called two-phase multipliers and X is called Martinelli parameter. $\left({}^{dP}/_{dy}\right)_{f,l}$ is the frictional pressure gradient assuming the liquid flows alone in the tube, $\left({}^{dP}/_{dy}\right)_{f,g}$ the frictional pressure gradient assuming the gas flows alone in the tube and $\left({}^{dP}/_{dy}\right)_f$ the actual frictional pressure gradient. $\left({}^{dP}/_{dy}\right)_{f,g}$ and $\left({}^{dP}/_{dy}\right)_{f,l}$ are computed as:

$$\left(\frac{dP}{dy}\right)_{f,l} = \frac{f_l G^2 (1-x_g)^2}{2\rho_l D_h}, \tag{33}$$

$$\left(\frac{dP}{dy}\right)_{f,g} = \frac{f_g G^2 x_g^2}{2\rho_g D_h}, \tag{34}$$

with f_g and f_l the gas and liquid friction factors, obtained from:

$$f_l = \frac{96}{Re_l}\,, \tag{35}$$

$$f_g = \frac{96}{Re_g}\,. \tag{36}$$

$\left({}^{dP}/_{dy}\right)_f$ is computed as:

$$\left(\frac{dP}{dy}\right)_f = \left(\frac{dP}{dy}\right)_t - \left(\frac{dP}{dy}\right)_a\,, \tag{37}$$

with $\left({}^{dP}/_{dy}\right)_t$ the total pressure gradient, obtained from the variable P solved by the code, and $\left({}^{dP}/_{dy}\right)_a$ the acceleration pressure gradient, obtained from the expression proposed by Martinelli and Nelson (1948):

$$\left(\frac{dP}{dy}\right)_a = G^2 \frac{d}{dy}\left(\frac{x_g^2}{\alpha_g \rho_g} + \frac{(1-x_g)^2}{(1-\alpha_g)\,\rho_l}\right)\,. \tag{38}$$

The multiplier ϕ_l^2 given by Eq. (30) is compared with that given by:

$$\phi_l^2 = 1 + \frac{C}{X} + \frac{1}{X^2}\,, \tag{39}$$

with X obtained from Eq. (32) and C obtained from the correlations in Table 8. These correlations have been established using data points coming from phase change experiments conducted in mini-channels. The correlations used are those of Hwang and Kim (2006), Kim and Mudawar (2012), Li and Wu (2010), Mishima and Hibiki (1996) and Zhang et al. (2010). An additional correlation, corresponding to the average of the previous ones, is employed. In the following, the multiplier ϕ_l^2 given by Eq. (30) is denoted $\phi_{l,num}^2$ while that given by Eq. (39) is denoted $\phi_{l,exp}^{2\,k}$, $k \in [\![1,6]\!]$. $\phi_{l,num}^2$ and $\phi_{l,exp}^{2\,k}$, $k \in [\![1,6]\!]$ are averaged over time. The mean relative error is computed as:

$$\mathrm{MRE}_k = \frac{1}{8}\sum_{i=1}^{8}\frac{1}{N_y}\sum_{j=1}^{N_y}\frac{\phi_{l,num}^2 - \phi_{l,exp}^{2\,k}}{\phi_{l,exp}^{2\,k}}\,, \tag{40}$$

with N_y the number of points (cells) in the y-direction.

4.2.2. Discussion of the results

Figs. 8 and 9 show, respectively, $\phi_{l,num}^2$ and the flow quality as a function of y for all the calculations performed. $\phi_{l,num}^2$ decreases to unity as the flow quality, inversely related to the amount of liquid, decreases to zero, which is consistent. At given y, $\phi_{l,num}^2$ increases with flow rate, due to the fact that the flow quality increases and thus the amount of liquid decreases.

Fig. 10 shows $\phi_{l,num}^2$ and $\phi_{l,exp}^{2\,k}$, $k \in [\![1,6]\!]$ as a function of y for Calculations 1 to 4. $\phi_{l,num}^2$ agrees qualitatively well with $\phi_{l,exp}^{2\,k}$, $k \in [\![1,6]\!]$.

The mean relative error is given in Table 9 and shown on the parity plot in Fig. 11. It is interesting to observe the relatively good accuracy of the correlation of Mishima and Hibiki (1996), which does not depend on the flow characteristics (it does not depend on any dimensionless number)

and is, in principle, not suited for horizontal configurations. A very good agreement is obtained with the correlation of Zhang et al. (2010). However, it is difficult to know if this correlation is more reliable than the others. Indeed, it is one of the most appropriate in terms of fluids and number of data points but one of the least appropriate in terms of diameter. Overall, the mean relative error is comprised between $-26.8\,\%$ and $27.3\,\%$, which is comparable with the values found in the literature for pressure drop. The mean relative error obtained with the average correlation is $0.289\,\%$, which is very low. Therefore, the frictional pressure drop and more globally flow dynamics is considered to be well predicted by the model.

4.3. Nusselt number

4.3.1. Computation and correlations used for comparison

In this section, the Nusselt number is computed as:

$$Nu_{tp} = \frac{h_{tp} D_h}{\lambda_b}\,, \tag{41}$$

with h_{tp} the two-phase heat transfer coefficient, obtained from:

$$h_{tp} = \frac{\varphi_{w\to g} + \varphi_{w\to l}}{T_w - T_b}\,. \tag{42}$$

$\varphi_{w\to g}$ and $\varphi_{w\to l}$ are given in Section 2.3.4 and T_w is given in Table 4. The bulk thermal conductivity λ_b and the bulk temperature T_b are given by:

$$\lambda_b = \frac{1}{d}\int_x \left(\alpha_g \lambda_g + \alpha_l \lambda_l\right) \mathrm{d}x\,, \tag{43}$$

$$T_b = \frac{\int_x \left(\alpha_g \rho_g Cp_g T_g + \alpha_l \rho_l Cp_l T_l\right) \mathrm{d}x}{\int_x \left(\alpha_g \rho_g Cp_g + \alpha_l \rho_l Cp_l\right) \mathrm{d}x}\,. \tag{44}$$

As previously, a comparison is made with experimental correlations. The correlations used, provided in Table 10, are those of Chato (1962), Kaushik and Azer (1988), Shah (2009) and Singh et al. (1996). Since they originally not depend on the amount of air, as usually done in the literature, they are weighted by a so-called degradation factor, denoted f_{nc}. The latter is obtained from the expression proposed by Kunh et al. (1997):

$$f_{nc} = f_{nc,1} f_{nc,2}\,, \tag{45}$$

with $f_{nc,1}$ and $f_{nc,2}$ given by:

$$f_{nc,1} = \frac{\delta_{Nu}}{\delta_{shear}}\left(1 + 7.32\times 10^{-4} Re_l\right)\,, \tag{46}$$

$$f_{nc,2} = \begin{cases} \left(1 - 2.601 Y_a^{0.708}\right) & \text{if } Y_a < 0.1 \\ \left(1 - Y_a^{0.292}\right) & \text{otherwise} \end{cases}\,, \tag{47}$$

$\delta_{Nu}/\delta_{shear}$ being the ratio of liquid film thickness with interfacial shear to film thickness without interfacial shear, assumed to be close to unity here due to small shear stress at the interface. An

Table 8: Correlations for C in Eq. (39). The corresponding ϕ_l^2 is denoted $\phi_{l,exp}^{2\,k}$, $k \in [\![1, 6]\!]$.

Correlation	D_h [mm]	Fluid(s)	Points	Expression for C
Hwang and Kim (2006)	0.244–0.792	R134a	77	$0.227 Re_{lo}^{0.452} X^{-0.32} N^{-0.82}$
Kim and Mudawar (2012)	0.0695–6.22	22 fluids	7115	$3.5 \times 10^{-5} Re_{lo}^{0.44} La_g^{0.5} \left(\frac{\rho_l}{\rho_g}\right)^{0.48}$
Li and Wu (2010)	0.148–3.25	12 fluids	769	$11.9 Bo^{0.45}$
Mishima and Hibiki (1996)	1.05–4.08	Air-Water	299	$21\left(1 - e^{-0.319 D_h}\right)$
Zhang et al. (2010)	0.07–6.2	10 fluids	2201	$21\left(1 - e^{-0.358/N}\right)$
Average correlation	–	–	–	–

$Bo = {g(\rho_l - \rho_g) D_h^2}/{\sigma}$ (Bond number); $La_g = {\rho_g \sigma D_h}/{\mu_g^2}$ (Laplace number based on gas); $N = \sqrt{{\sigma}/{g(\rho_l - \rho_g) D_h^2}}$ (confinement number); $Re_{lo} = {G D_h}/{\mu_l}$ (Reynolds number assuming only liquid).

Table 9: Mean relative error (MRE) on ϕ_l^2 (Eq. (40)).

Correlation	MRE [%]
Hwang and Kim (2006)	15.7
Kim and Mudawar (2012)	16.2
Li and Wu (2010)	−26.8
Mishima and Hibiki (1996)	27.3
Zhang et al. (2010)	−8.36
Average correlation	0.289

additional correlation, corresponding to the average of the previous ones, is employed. In the following, the Nusselt number obtained from Eqs. (41) to (44) is denoted $Nu_{tp,num}$ while that obtained from the correlations in Table 10 is denoted $Nu^k_{tp,exp}$, $k \in [\![1,5]\!]$. $Nu_{tp,num}$ and $Nu^k_{tp,exp}$, $k \in [\![1,5]\!]$ are averaged over time. The mean relative error is computed as:

$$\mathrm{MRE}_k = \frac{1}{8}\sum_{i=1}^{8}\frac{1}{N}\sum_{j=1}^{N}\frac{Nu_{tp,num} - Nu^k_{tp,exp}}{Nu^k_{tp,exp}}\,. \tag{48}$$

4.3.2. Discussion of the results

Fig. 12 shows $Nu_{tp,num}$ as a function of y for all the calculations performed. The profiles can be decomposed into four regions: two developing regions, where $Nu_{tp,num}$ decreases, and two developed regions, where $Nu_{tp,num}$ is constant or almost constant. The transition from the first developed region to the second developing region occurs when $\alpha_l \gg \alpha_g$ and thus $\varphi_w \approx \varphi_{w\to l}$, $\lambda_b \approx \frac{1}{d}\int_x \alpha_l\lambda_l \mathrm{d}x$ and $T_b \approx \int_x \alpha_l\rho_l Cp_l T_l \mathrm{d}x / \int_x \alpha_l\rho_l Cp_l \mathrm{d}x$. The constant value reached by $Nu_{tp,num}$ in the developed regions is close to that predicted by single-phase flow theory (see the single-phase flow verification performed in Section 3.7). At given y in the entrance region (first developing region), $Nu_{tp,num}$ increases with flow rate, due to the fact that both φ_{cond} and $\varphi_{sp,g}$ increase.

Fig. 13 shows $Nu_{tp,num}$ and $Nu^k_{tp,exp}$, $k \in [\![1,5]\!]$ as a function of y for Calculations 1 to 4. Since the correlations assume the flow to be fully developed, $Nu^k_{tp,exp}$, $k \in [\![1,5]\!]$ is only shown in the second developed region (see paragraph above). Qualitatively speaking, a good agreement is obtained between $Nu_{tp,num}$ and $Nu^k_{tp,exp}$, $k \in [\![1,5]\!]$.

The mean relative error is given in Table 11 and shown on the parity plot in Fig. 14. Excellent agreement is obtained with the correlation of Chato (1962). This correlation is considered to be the most reliable for the present calculations. Indeed, it is completely based on the analytical solution of Nusselt (1916) for laminar condensation on a plate. The worst agreement is obtained with the correlation of Shah (2009). However, less confidence is placed in this correlation than in the others. Indeed, even if few authors, such as Borchman (1967), have found it to give acceptable predictions in the laminar flow regime, the fact remains that it has originally not been developed for laminar flows (a large part of the data on which it is based corresponds to the turbulent flow regime). Excluding this correlation, the mean relative error is comprised between $-35.3\,\%$ and $37.2\,\%$, which is of the same order of what can be found in the literature. The mean relative error obtained with the average correlation is $-13.4\,\%$, which is reasonable. Therefore, the Nusselt number and more generally heat transfer is considered to be correctly predicted by the model.

4.4. Generalization of the results obtained for the Nusselt number

The purpose of this section is to find a relevant dimensionless coordinate for plotting the Nusselt number defined by Eqs. (41) to (44). As shown in Fig. 15, the dimensionless coordinate ${}^{4y}/_{D_h Re_g Pr_g}$ used for single-phase flow (see Section 3.7) is not appropriate. Indeed, the curves corresponding to

Table 10: Correlations for the Nusselt number. The corresponding Nusselt number is denoted $Nu^k_{tp,exp}$, $k \in [\![1,5]\!]$.

Correlation	D_h [mm]	Fluid(s)	Points	Expression for $Nu_{tp,exp}$
Chato (1962)	14.5–27.9	Air-Water, R113	n/a	$f_{nc} \cdot 0.555 \left(\frac{GaPr_l}{Ja}\right)^{1/4}$
Kaushik and Azer (1988)	12.5–17.8	R11, R113	n/a	$f_{nc} \cdot 2.078 Re_{eq}^{0.507} Pr_l^{1/3} \left(\frac{\Delta x_g D_h}{l}\right)^{0.198} P_r^{-0.14}$
Shah (2009)	2–49	17 fluids	1189	$f_{nc} \cdot \left[0.023 Re_{lo}^{0.8} Pr_l^{0.4} \left(\frac{\mu_l}{14\mu_g}\right)^n \alpha + 1.32 Re_{lo}^{-1/3} Ga^{1/3}\right]$
Singh et al. (1996)	11	R134a	n/a	$f_{nc} \cdot \left[0.2339 Re_l^{0.5} Pr_l^{0.33} \theta + 0.0925 \left(\frac{GaPr_l}{Ja}\right)^{1/4} (2\pi - \theta)\right]$
Average correlation	–	–	–	–

$Ga = {g\rho_l(\rho_l - \rho_g)D_h^3}/{\mu_l^2}$ (Galileo number); $Ja = {Cp_l(T_{sat} - T_w)}/{H_{lat}}$ (Jakob number); $n = 0.0058 + 0.557 P_r$ (exponent); $P_r = {P}/{P_c}$ with P_c the critical pressure (reduced pressure); $Re_{eq} = {G_{eq} D_h}/{\mu_l}$ with $G_{eq} = G(1 - x_g) + G x_g \sqrt{{\rho_l}/{\rho_g}}$ (equivalent Reynolds number); $\alpha = (1 - x_g)^{0.8} + {3.8 x_g^{0.76} (1 - x_g)^{0.04}}/{P_r^{0.38}}$ (coefficient); $\Delta x_g = x_g^{in} - x_g^{out}$ (flow quality variation); $\theta = 2 \arccos(2\alpha_g - 1)$ (coefficient).

Table 11: Mean relative error (MRE) on the Nusselt number (Eq. (48)).

Correlation	MRE [%]
Chato (1962)	−6.77
Kaushik and Azer (1988)	−18.8
Shah (2009)	37.2
Singh et al. (1996)	−35.3
Average correlation	−13.4

Calculations 1 to 4, characterized by $T_g^{in} - T_w = 27\,\mathrm{K}$, do not overlap with those corresponding to Calculations 4 to 8, characterized by $T_g^{in} - T_w = 37\,\mathrm{K}$. This is due to condensation, which depends on both T_g^{in} and T_w. Based on these considerations, the following new dimensionless coordinate is proposed:

$$y^* = \frac{4yJa^*}{D_h Re_g Pr_g}\,, \tag{49}$$

with Ja^* a modified Jakob number based on $T_g^{in} - T_w$:

$$Ja^* = \frac{Cp_l\left(T_g^{in} - T_w\right)}{H_{lat}}\,. \tag{50}$$

As shown is Fig. 16, this new dimensionless coordinate allows all the curves to overlap. An expression could be derived by curve fitting and could then be used for one-dimensional calculations. Note that this expression would only be valid for $Y_a^{in} = 0.01$ and $T_g^{in} - T_w > 27\,\mathrm{K}$. A more general analysis should be conducted to provide an expression valid for all values of Y_a^{in} and $T_g^{in} - T_w$.

5. Conclusion

A new model implemented in the neptune_cfd code was used to simulate steam condensation in the presence of air in a mini-channel of opening 100 µm. Various flow patterns, including droplet, smooth annular, wavy annular and slug flow, were observed. These flow patterns were found to be consistent in nature with those observed experimentally. The results were compared with various experimental correlations from the literature. The considered quantities were the pressure drop and the Nusselt number. They were predicted with minimal absolute mean relative errors of, respectively, 0.289 % and 13.4 %, which was considered indicative of a reasonably good accuracy of the model. The present work shows the relevance of the proposed model for the simulation of condensing two-phase flows in mini-channels, and more generally for the simulation of two-phase flows with phase change involving large deformable interfaces, small dispersed bubbles and small dispersed droplets. Its application to model cracks for the prediction of the leakage rate in the event of an accident is possible, but corresponding calculations would be time consuming, due to the fact that most of the accident scenarios last several days and that the dimensions of the problem imply the use of small time steps. A solution could be to perform 1D calculations, allowing for larger cells and thus larger time steps. The gas and liquid frictional pressure drops, as well as the gas and liquid wall heat fluxes, could be obtained from standard laws and the condensation flux deduced from the law $Nu_{tp} = f\left(y^*\right)$ proposed in Section 4.4.

Declaration of interests

The authors declare that they have no known competing financial interests or personal relationships that could have appeared to influence the work reported in this paper.

Acknowledgements

This work has been achieved in the framework of the CIWAP3 project, financially supported by EDF. The neptune_cfd code is being developed in the framework of the NEPTUNE project, financially supported by EDF, Commissariat à l'Energie Atomique et aux Energies Alternatives (CEA), Institut de Radioprotection et de Sûreté Nucléaire (IRSN) and Framatome.

Nomenclature

Roman letters		
a^{int}	Interfacial area concentration	m^{-1}
A_l	Fraction of area affected by the liquid	–
c	Rescaling factor for h_{loc}	–
C	Force coefficient	–
Cp	Specific heat capacity	$\mathrm{J\,kg^{-1}\,K^{-1}}$
d	Diameter	m
D	Diffusion coefficient	$\mathrm{m^2\,s^{-1}}$
D_h	Hydraulic diameter	m
f	Friction factor	–
$f_{nc}, f_{nc,1}, f_{nc,2}$	Degradation factor	–
f^θ	Function for drag computation	$\mathrm{kg\,m^{-3}\,s^{-1}}$
F	Force density	$\mathrm{kg\,m^{-2}\,s^{-2}}$
g	Gravity	$\mathrm{m\,s^{-2}}$
G	Mass flow rate per unit area	$\mathrm{kg\,m^{-2}\,s^{-1}}$
h	Heat transfer coefficient	$\mathrm{W\,m^{-2}\,K^{-1}}$
H	Average total enthalpy	$\mathrm{J\,kg^{-1}}$
I	Interfacial momentum transfer	$\mathrm{kg\,m^{-2}\,s^{-2}}$
Ja^*	Modified Jakob number	–
MRE	Mean relative error	–
n	Interface normal	–
n_{site}	Number of droplets per unit area	$\mathrm{m^{-2}}$
Nu	Nusselt number	–
P	Pressure	Pa
Pr	Prandtl number	–
Q	Heat flux density	$\mathrm{W\,m^{-2}}$
Re	Reynolds number	–
S/V	Surface-to-volume ratio	$\mathrm{m^{-1}}$
Sc	Schmidt number	–
Sh	Sherwood number	–
T	Temperature	K
U	Average velocity	$\mathrm{m\,s^{-1}}$
x, y, z	Cartesian coordinates	m
X	Martinelli parameter	–
x_g	Flow quality	–
Y	Mass fraction	–

y^*	Dimensionless y-coordinate	–

Greek letters		
α	Volume fraction	–
Γ	Interfacial mass transfer	$\mathrm{kg\,m^{-3}\,s^{-1}}$
Δ	Distance from wall to center of boundary cell	m
Δt	Time step	s
Δx, Δy, Δz	Grid spacing in x-, y-, z-direction	m
ε	Interface sharpening coefficient	m
θ	Drag relaxation coefficient	–
λ	Thermal conductivity	$\mathrm{W\,m^{-1}\,K^{-1}}$
μ	Molecular viscosity	$\mathrm{kg\,m^{-1}\,s^{-1}}$
Π	Interfacial energy transfer	$\mathrm{W\,m^{-3}}$
ρ	Density	$\mathrm{kg\,m^{-3}}$
σ	Surface tension	$\mathrm{kg\,s^{-2}}$
Σ	Stress tensor	$\mathrm{kg\,m^{-1}\,s^{-2}}$
τ	Characteristic time for bubbles	s
φ	Wall energy transfer	$\mathrm{W\,m^{-2}}$
ϕ^2	Two-phase multiplier	–

Subscripts and superscripts		
a	Air	–
AM	Added mass	–
b	Bulk	–
c	Continuous	–
$cond$	Condensation	–
d	Dispersed	–
D	Drag	–
exp	Experimental	–
g	Gas	–
in	Inlet	–
inf	Inferior	–
int	Interfacial	–
l	Liquid	–
L	Lift	–
lat	Latent	–
lim	Limit	–
loc	Local	–
num	Numerical	–
out	Outlet	–
pl	Liquid particle	–
pg	Gas particle	–
q	Quenching	–
Re	Reynolds	–
s	Steam	–
sp	Single-phase	–
sat	Saturation	–
ST	Surface tension	–
sup	Superior	–
TD	Turbulent dispersion	–
tot	Total	–
tp	Two-phase	–
w, W	Wall	–
x, y, z	x-, y-, z-component	–

References

Borchman, J., 1967. Heat transfer of high velocity vapor condensing in annuli. ASHRAE Trans. 73.

Brackbill, J.U., Kothe, D.B., Zemach, C., 1992. A continuum method for modeling surface tension. J. Comput. Phys. 100, 335–54.

Brauner, N., Moalem-Maron, D., 1992. Identification of the range of 'small diameters' conduits, regarding two-phase flow pattern transitions. Int. Commun. Heat Mass Transf. 19, 29–39.

Carey, V.P., 1992. Liquid-vapor phase change phenomena: An introduction to the thermophysics of vaporization and condensation process in heat transfer equipment. Hemisphere.

Chato, J.C., 1962. Laminar condensation in horizontal and inclined tubes. ASHRAE J. 4, 52–60.

Chen, M., Yang, Z., Duan, Y., Chen, Y., Wu, D., 2014. Simulation of condensation flow in a rectangular microchannel. Int. Commun. Heat Mass Transf. 76, 60–9.

Cornwell, K., Kew, P.A., 1993. Boiling in small parallel channels. Elsevier Applied Science.

Coste, P., 2013. A large interface model for two-phase CFD. Nucl. Eng. Des. 255, 38–50.

Coste, P., Lavieville, J., 2008. A two-phase approach to the PTS problem evaluated on COSI experiment. 16th International Conference on Nuclear Engineering (ICONE-16), Orlando, USA.

Coste, P., Lavieville, J., 2009. A wall function-like approach for two-phase CFD condensation modeling of the pressurized thermal shock. 13th International Topical Meeting on Nuclear Reactor Thermal Hydraulics (NURETH-13), Kanazawa, Japan.

Da Riva, E., Del Col, D., 2011. Effect of gravity during condensation of R134a in a circular minichannel. Microgravity Sci. Technol. 23, 87–97.

Da Riva, E., Del Col, D., 2012. Numerical simulation of laminar liquid film condensation in a horizontal circular minichannel. J. Heat Transf. 134, 051019.

Da Riva, E., Del Col, D., Garimella, S.V., Cavallini, A., 2012. The importance of turbulence during condensation in a horizontal circular minichannel. Int. J. Heat Mass Transf. 55, 3470–81.

Davy, G., Reyssat, E., Vincent, S., Mimouni, S., 2020. CFD modeling of two-phase flows in cracks. 8th Workshop on Computational Fluid Dynamics for Nuclear Reactor Safety (CFD4NRS-8), Paris, France.

Denèfle, R., Mimouni, S., Caltagirone, J.P., Vincent, S., 2015. Multifield hybrid approach for two-phase flow modeling – Part 1: Adiabatic flows. Comput. Fluids 113, 106–11.

Emonot, P., Souyri, A., Grandrille, J.L., Barré, F., 2011. CATHARE-3: A new system code for thermal-hydraulics in the context of the NEPTUNE project. Nucl. Eng. Des. 241, 4476–81.

Fleau, S., 2017. Multifield approach and interface locating method for two-phase flows in nuclear power plant. Ph.D. thesis. Université Paris-Est.

Fleau, S., Mimouni, S., Mérigoux, N., Vincent, S., 2015. Validation of multifield approach for the simulations of two-phase flows. Comput. Therm. Sci. 7, 441–57.

Ganapathy, H., Shooshtari, A., Choo, K., Dessiatoun, S., Alshehhi, M., Ohadi, M., 2013. Volume of fluid-based numerical modeling of condensation heat transfer and fluid flow characteristics in microchannels. Int. J. Heat Mass Transf. 65, 62–72.

Gobin, A., Neau, H., Simonin, O., Llinas, J.R., Reiling, V., Selo, J.L., 2003. Fluid dynamic numerical simulation of a gas phase polymerization reactor. Int. J. Numer. Methods Fluids 43, 1199–220.

Guelfi, A., Bestion, D., Boucker, M., Boudier, P., Fillion, P., Grandotto, M., Hérard, J.M., Hervieu, E., Péturaud, P., 2007. NEPTUNE: A new software platform for advanced nuclear thermal hydraulics. Nucl. Sci. Eng. 156, 281–324.

Hu, J.S., Chao, C.Y.H., 2007. An experimental study of the fluid flow and heat transfer characteristics in micro-condensers with slug-bubbly flow. Int. J. Refrig. 30, 1309–18.

Hwang, Y.W., Kim, M.S., 2006. The pressure drop in microtubes and the correlation development. Int. J. Heat Mass Transf. 49, 1804–12.

Ishii, M., Zuber, N., 1979. Drag coefficient and relative velocity in bubbly, droplet or particulate flows. AIChE J. 25, 843–55.

Kaushik, N., Azer, N.Z., 1988. A general heat transfer correlation for condensation inside internally finned tubes. ASHRAE Trans. 94, 261–79.

Kays, W.M., Crawford, M.E., 1993. Convection heat and mass transfer. McGraw-Hill.

Kim, S.M., Kim, J., Mudawar, I., 2012. Flow condensation in parallel micro-channels – Part 1: Experimental results and assessment of pressure drop correlations. Int. J. Heat Mass Transf. 55, 971–83.

Kim, S.M., Mudawar, I., 2012. Universal approach to predicting two-phase frictional pressure drop for adiabatic and condensing mini/micro-channel flows. Int. J. Heat Mass Transf. 55, 3246–61.

Kunh, S.Z., Schrock, V.E., Peterson, P.F., 1997. An investigation of condensation from steam-gas mixture flow downward inside a vertical tube. Nucl. Eng. Des. 177, 53–69.

Lee, W.H., 1980. A pressure iteration scheme for two-phase flow modeling. Hemisphere.

Li, W., Wu, Z., 2010. A general correlation for adiabatic two-phase pressure drop in micro/mini-channels. Int. J. Heat Mass Transf. 53, 2732–9.

Lockhart, R.W., Martinelli, R.C., 1947. Proposed correlation of data for isothermal two-phase, two-component flow in pipes. Chem. Eng. Prog. 45, 39–48.

Manon, E., 2000. Contribution à l'analyse et à la modélisation locale des écoulements bouillants sous-saturés dans les conditions des Réacteurs à Eau sous Pression. Ph.D. thesis. Ecole Centrale Paris.

Martinelli, R.C., Nelson, B., 1948. Prediction of pressure drop during forced-circulation boiling water. Trans. ASME 70, 695–702.

Mer, S., Praud, O., Neau, H., Mérigoux, N., Magnaudet, J., Roig, V., 2018. The emptying of a bottle as a test case for assessing interfacial momentum exchange models for Euler–Euler simulations of multi-scale gas-liquid flows. Int. J. Multiph. Flow 106, 109–24.

Mercer, W.E., Pearce, W.M., Hitchcock, J.E., 1967. Laminar forced convection in the entrance region between parallel flat plates. J. Heat Transf. 89, 251–6.

Mérigoux, N., Lavieville, J., Mimouni, S., Guingo, M., Baudry, C., 2016. A generalized large interface to dispersed bubbly flow approach to model two-phase flows in nuclear power plant. 6th Workshop on Computational Fluid Dynamics for Nuclear Reactor Safety (CFD4NRS-6), Cambridge, USA.

Mimouni, S., Baconnier, P., Davy, G., 2019. Overview of mitigation models dedicated to severe accidents and consequences on flow rate through concrete containment structures. 18th International Topical Meeting on Nuclear Reactor Thermal Hydraulics (NURETH-18), Portland, USA.

Mimouni, S., Fleau, S., Vincent, S., 2017. CFD calculations of flow pattern maps and LES of multiphase flows. Nucl. Eng. Des. 321, 118–31.

Mimouni, S., Foissac, A., Lavieville, J., 2011. CFD modelling of wall steam condensation by a two-phase flow approach. Nucl. Eng. Des. 241, 4445–55.

Mimouni, S., Lamy, J.S., Lavieville, J., Guieu, S., Martin, M., 2010. Modelling of sprays in containment applications with a CMFD code. Nucl. Eng. Des. 240, 2260–70.

Mishima, K., Hibiki, T., 1996. Some characteristics of air-water two-phase flow in small diameter vertical tubes. Int. J. Multiph. Flow 22, 703–12.

Nusselt, W., 1916. Die oberflachenkondensation des wasserdampfes. Z. Ver. D. Ing. 60, 541–6.

Oran, E.S., Boris, J.P., 1981. Detailed modelling of combustion systems. Prog. Energy Combust. Sci. 7, 1–72.

Ranz, W.E., Marshall, W.R., 1952. Evaporation from drops. Chem. Eng. Prog. 48, 141–6.

Rastiello, G., Leclaire, S., Belarbi, R., Bennacer, R., 2015. Unstable two-phase flow rate in micro-channels and cracks under imposed pressure difference. Int. J. Multiph. Flow 77, 131–41.

Ruyer, P., Seiler, N., Weiss, M., Weiss, F.P., 2007. A bubble size distribution model for the simulation of bubbly flows. 6th International Conference on Multiphase Flow (ICMF-6), Leipzig, Germany.

Shah, M.M., 2009. An improved and extended general correlation for heat transfer during condensation in plain tubes. HVAC&R Res. 15, 889–913.

Singh, A., Ohadi, M.M., Dessiatoun, S.V., 1996. Empirical modeling of stratified-wavy flow condensation heat transfer in smooth horizontal tubes. ASHRAE Trans. 102, 596–603.

Suo, M., Griffith, P., 1964. Two-phase flow in capillary tubes. J. Basic Eng. 86, 576–82.

Tomiyama, A., Tamai, H., Zun, I., Hosokawa, S., 2002. Transverse migration of single bubbles in simple shear flows. Chem. Eng. Sci. 57, 1849–58.

Wang, W.W., Radcliff, T.D., Christensen, R.N., 2002. A condensation heat transfer correlation for millimeter-scale tubing with flow regime transition. Exp. Therm. Fluid Sci. 26, 473–85.

Wu, C., Cheng, P., 2005. Condensation flow patterns in silicon microchannels. Int. J. Heat Mass Transf. 48, 2186–97.

Yin, Z., Guo, Y., Suden, B., Wang, Q., Zeng, M., 2015. Numerical simulation of laminar film condensation in a horizontal minitube with and without non-condensable gas by the VOF method. Numer. Heat Tr. A-Appl. 68, 958–77.

Zhang, J., Li, W., Minkowycz, W.J., 2016a. Numerical simulation of condensation for R410A at varying saturation temperatures in mini/micro tubes. Numer. Heat Tr. A-Appl. 69, 464–78.

Zhang, J., Li, W., Minkowycz, W.J., 2017. Numerical simulation of R410A condensation in horizontal microfin tubes. Numer. Heat Tr. A-Appl. 71, 361–76.

Zhang, J., Li, W., Sherif, S.A., 2016b. A numerical study of condensation heat transfer and pressure drop in horizontal round and flattened minichannels. Int. J. Therm. Sci. 106, 80–93.

Zhang, W., Hibiki, T., Mishima, K., 2010. Correlations of two-phase frictional pressure drop and void fraction in mini-channel. Int. J. Heat Mass Transf. 53, 453–65.

Zhao, Z., Zhang, Y., Chen, X., Ma, X., Yanga, S., Li, S., 2015. A numerical study on condensation flow and heat transfer of refrigerant in minichannels of printed circuit heat exchanger. Int. J. Refrig. 102, 96–111.

Zuber, N., 1964. On the dispersed two-phase flow in the laminar flow regime. Chem. Eng. Sci. 19, 897–917.

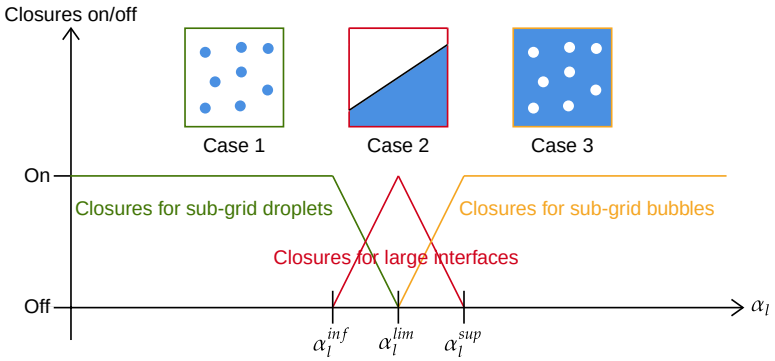

Figure 1: Principle of the Full Generalized Large Interface Model. The model uses a sub-grid approach in Cases 1 and 3 and an interface capturing approach in Case 2. Closures for mass, momentum and energy used in Cases 1 and 3 come from the Standard Dispersed Model for droplets and the Standard Dispersed Model for bubbles, respectively. Those used in Case 2 come from the Large Interface Model. α_l^{inf}, α_l^{lim} and α_l^{sup} are set to 0.4, 0.5 and 0.6, respectively.

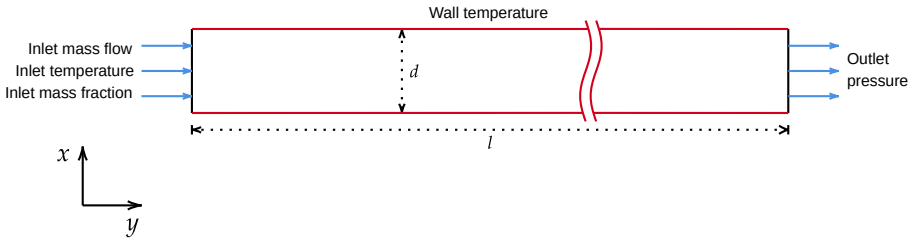

Figure 2: Computational domain and boundary conditions. Dimensions are: $d = 100\,\mu\text{m}$ and $l = 3\,\text{cm}$. Mass flow rate, temperature and composition are imposed at the inlet, pressure is imposed at the outlet and temperature is imposed at the walls.

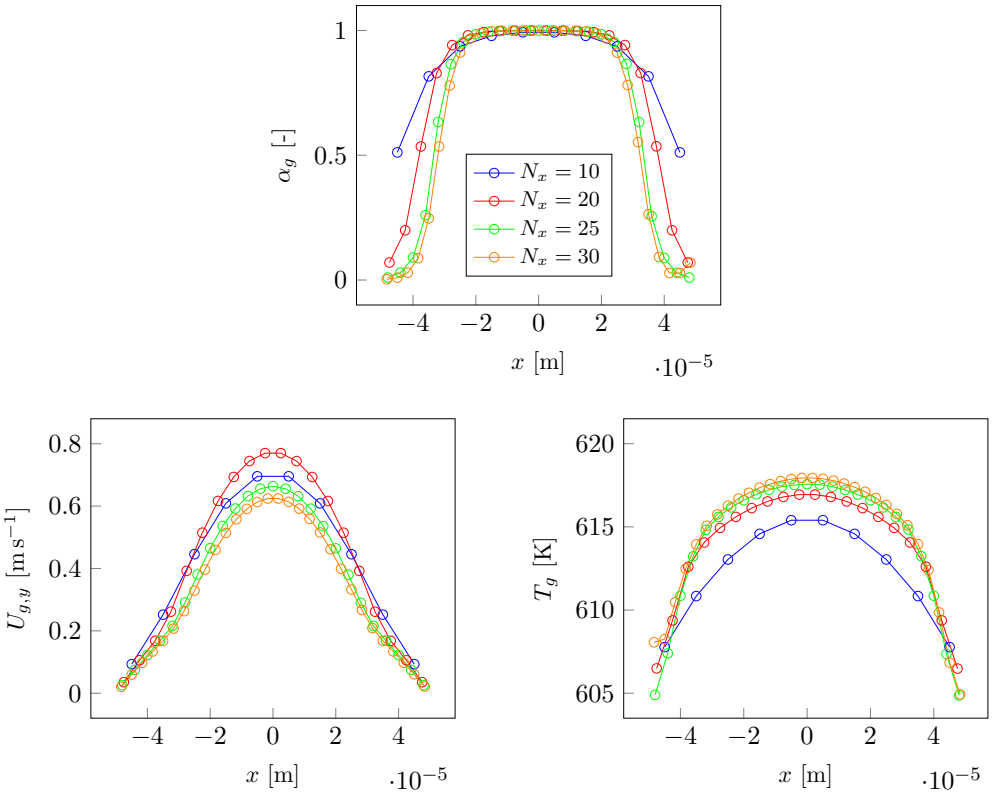

Figure 3: Permanent profiles of gas volume fraction (top), y-component of the gas velocity (bottom left) and gas temperature (bottom right) obtained in Calculation 4 at $y = 0.01\,\mathrm{m}$ for the various meshes studied

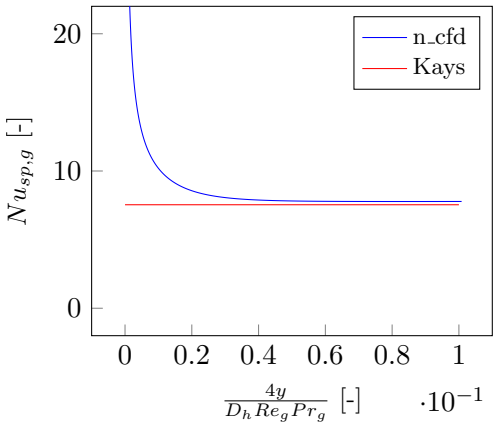

Figure 4: Evolution of $Nu_{sp,g}$ (Eqs. (26) and (27)) as a function of $^{4y}/_{Re_g Pr_g D_h}$. Comparison is made with the analytical solution of Kays and Crawford (1993) (Eq. (28)) in the fully developed region.

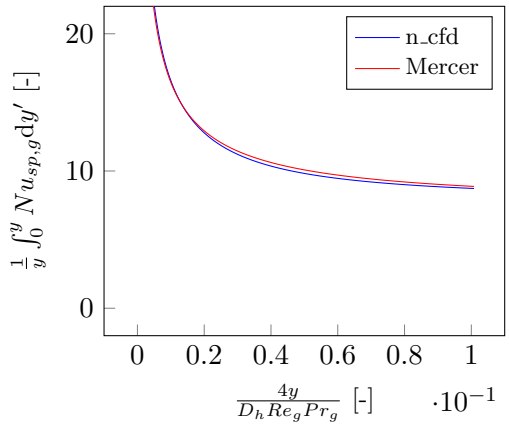

Figure 5: Evolution of $^1/_y \int_0^y Nu_{sp,g}\mathrm{d}y'$ (with $Nu_{sp,g}$ given by Eqs. (26) and (27)) as a function of $^{4y}/_{Re_g Pr_g D_h}$. Comparison is made with the analytical solution of Mercer et al. (1967) (Eq. (29)) in both the hydrodynamic and thermal developing region and the fully developed region.

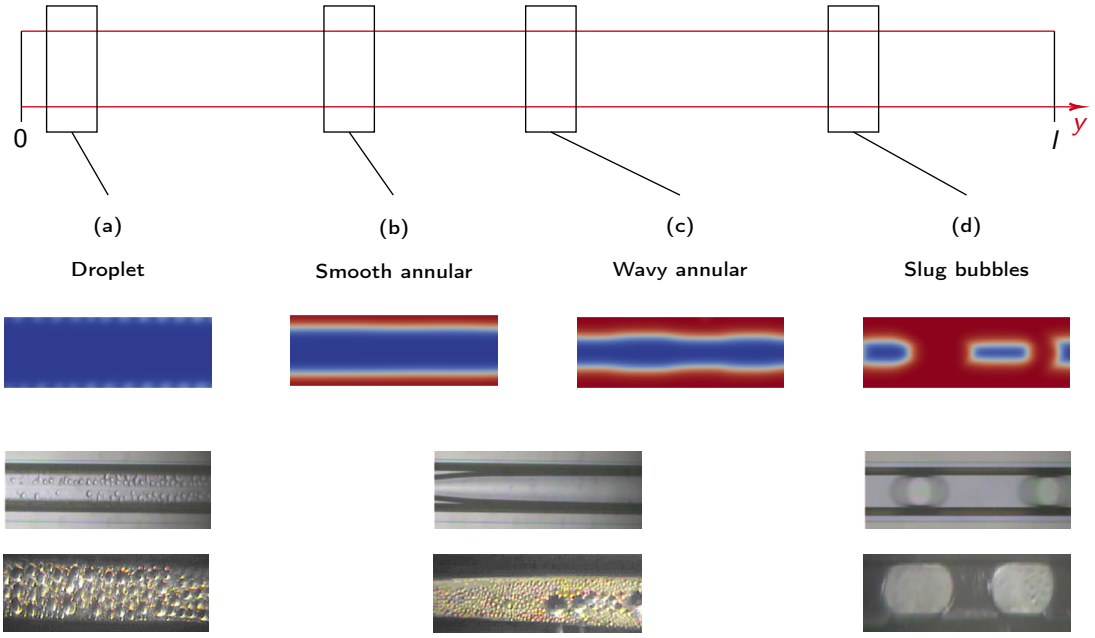

Figure 6: Flow patterns obtained in the present work (top line; gas in blue; liquid in red; flow from left to right). Qualitative comparison is made with the experiments of Wu and Cheng (2005) (middle line; flow from right to left) and Hu and Chao (2007) (bottom line; flow from right to left).

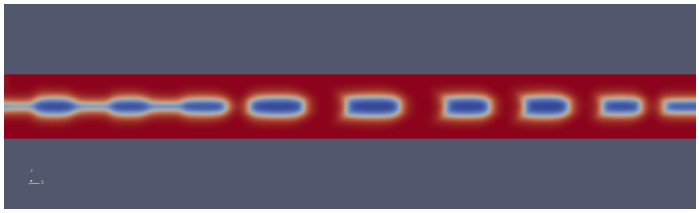

Figure 7: Transition from wavy annular to slug flow (gas in blue; liquid in red).

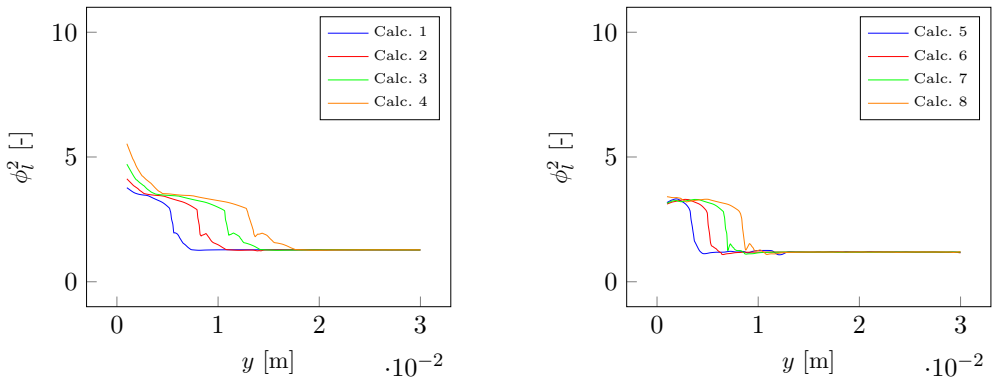

Figure 8: Evolution of $\phi^2_{l,num}$ (Eq. (30)) along the mini-channel for all the calculations performed (left axis range is based on Fig. 10).

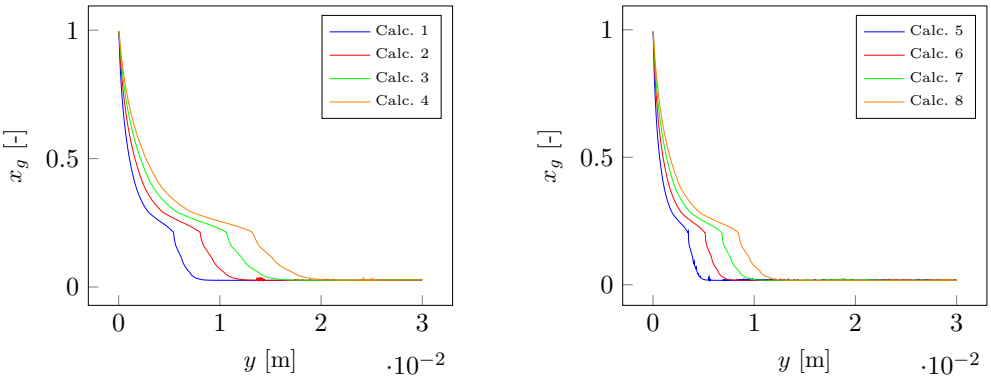

Figure 9: Evolution of the flow quality (Eq. (25)) along the mini-channel for all the calculations performed.

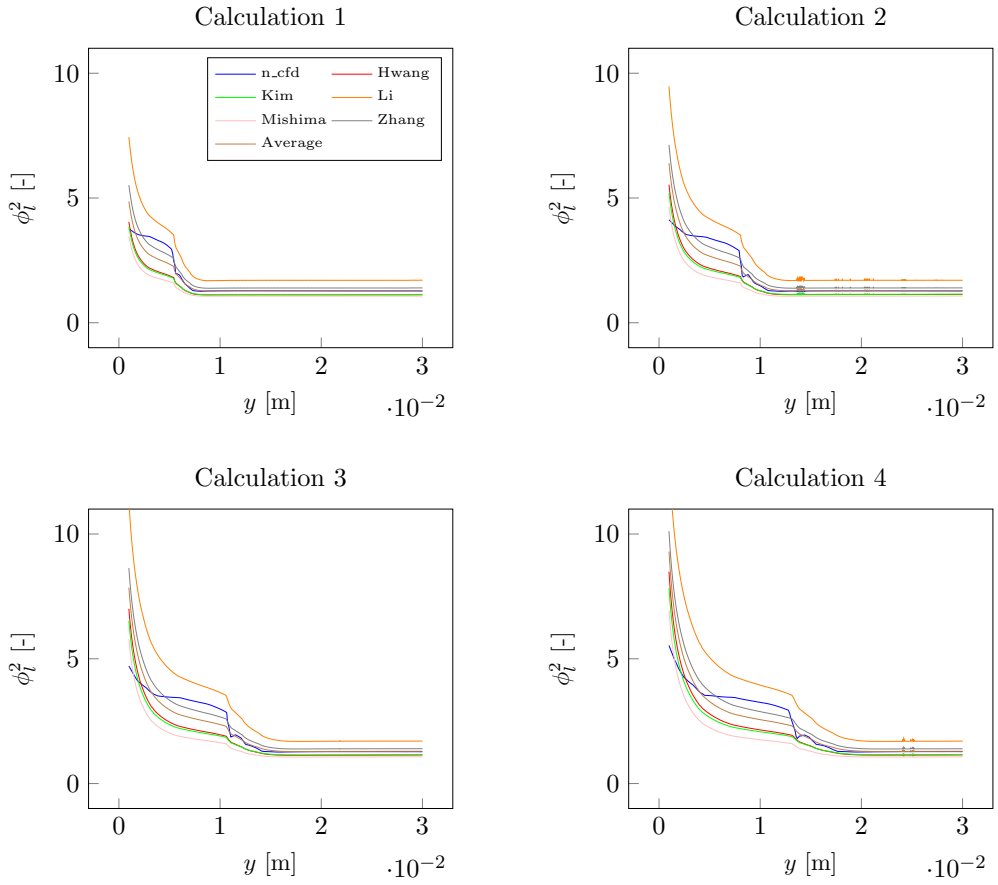

Figure 10: Comparison between $\phi^2_{l,num}$ and $\phi^{2\,k}_{l,exp}$, $k \in [\![1, 6]\!]$ for Calculations 1 to 4. $\phi^2_{l,num}$ is obtained from Eq. (30) while $\phi^{2\,k}_{l,exp}$, $k \in [\![1, 6]\!]$ is obtained from Eq. (39) and Table 8.

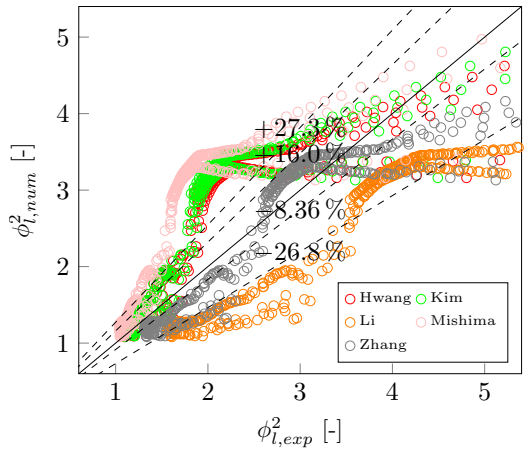

Figure 11: Parity plot of $\phi^{2\,k}_{l,exp}$, $k \in [\![1,6]\!]$ versus $\phi^2_{l,num}$ at various locations along the mini-channel. $\phi^2_{l,num}$ is obtained from Eq. (30) while $\phi^{2\,k}_{l,exp}$, $k \in [\![1,6]\!]$ is obtained from Eq. (39) and Table 8.

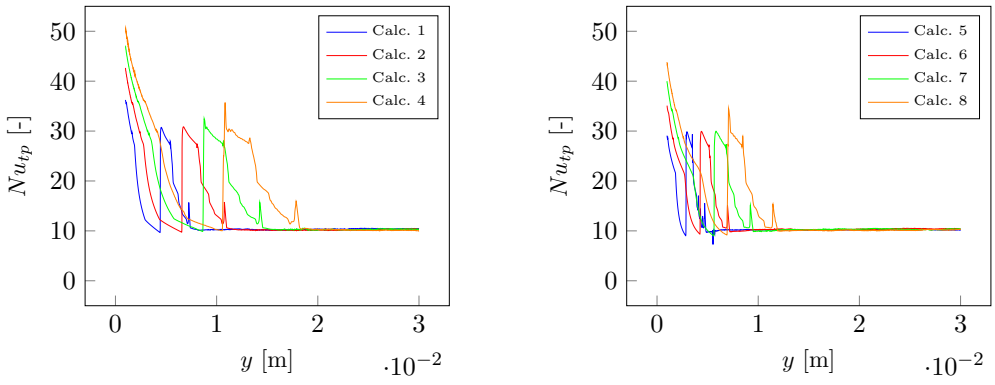

Figure 12: Evolution of $Nu_{tp,num}$ (Eqs. (41) to (44)) along the mini-channel for all the calculations performed.

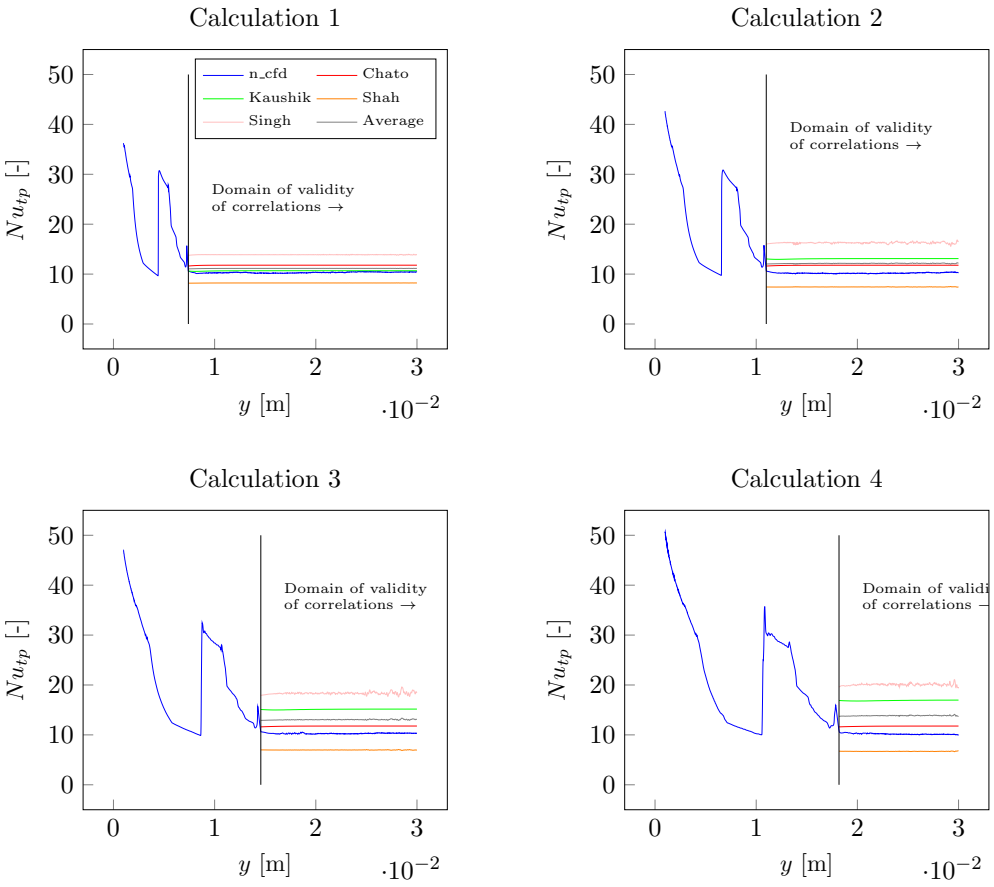

Figure 13: Comparison between $Nu_{tp,num}$ and $Nu^k_{tp,exp}$, $k \in [\![1,5]\!]$ for Calculations 1 to 4. $Nu_{tp,num}$ is obtained from Eqs. (41) to (44) while $Nu^k_{tp,exp}$, $k \in [\![1,5]\!]$ number is obtained from Table 10.

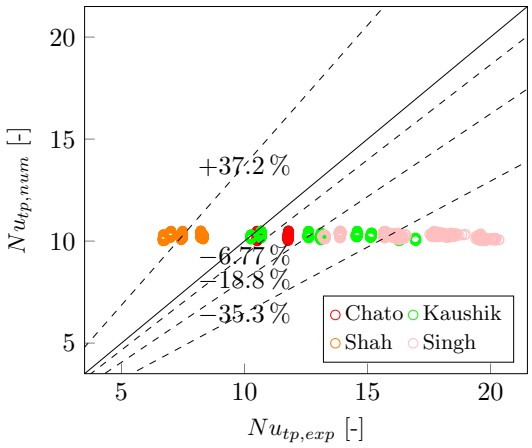

Figure 14: Parity plot of $Nu^k_{tp,exp}$, $k \in [\![1,5]\!]$ versus $Nu_{tp,num}$ at various locations along the mini-channel. $Nu_{tp,num}$ is obtained from Eqs. (41) to (44) while $Nu^k_{tp,exp}$, $k \in [\![1,5]\!]$ is obtained from Table 10.

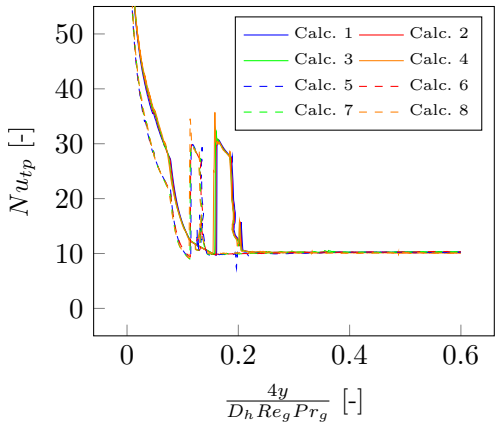

Figure 15: Evolution of $Nu_{tp,num}$ (Eqs. (41) to (44)) as a function of $^{4y}/_{Re_g Pr_g D_h}$ for all the calculations performed.

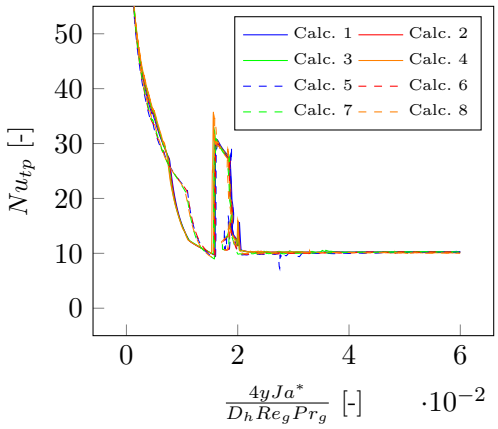

Figure 16: Evolution of $Nu_{tp,num}$ (Eqs. (41) to (44)) as a function of ${}^{4yJa^*}/_{Re_g Pr_g D_h}$ for all the calculations performed.